

# Hidden Weyl Points in Centrosymmetric Paramagnetic Metals

Dominik Gresch<sup>1</sup>, QuanSheng Wu<sup>1</sup>, Georg W. Winkler<sup>1</sup>, and Alexey A. Soluyanov<sup>1,2</sup>

<sup>1</sup>*Theoretical Physics and Station Q Zurich, ETH Zurich, 8093 Zurich, Switzerland and*

<sup>2</sup>*Department of Physics, St. Petersburg State University, St. Petersburg, 199034 Russia*

(Dated: January 20, 2017)

The transition metal dipnictides TaAs<sub>2</sub>, TaSb<sub>2</sub>, NbAs<sub>2</sub> and NbSb<sub>2</sub> have recently sparked interest for exhibiting giant magnetoresistance. While the exact nature of magnetoresistance in these materials is still under active investigation, there are experimental results indicating anisotropic negative magnetoresistance. We study the effect of magnetic field on the band structure topology of these materials by applying a Zeeman splitting. In the absence of magnetic field, we find that the materials are weak topological insulators, which is in agreement with previous studies. When the magnetic field is applied, we find that type - II Weyl points form. This result is found first from a symmetry argument, and then numerically for a  $\mathbf{k} \cdot \mathbf{p}$  model of TaAs<sub>2</sub> and a tight-binding model of NbSb<sub>2</sub>. This effect can be of help in search for an explanation of the anomalous magnetoresistance in these materials.

## I. INTRODUCTION

Weyl nodes are point-like crossings of two energy bands, with a linear dispersion. Locally, they can be described by Hamiltonian of the form

$$H(k) = \sum_{i,j} k_i A_{i,j} \sigma_j \quad (1)$$

where  $i \in \{x, y, z\}$ ,  $j \in \{0, x, y, z\}$ . Topologically, a Weyl node can be characterized by being a quantized source or sink of Berry curvature, depending on its chirality [1]. Due to this quantized nature, Weyl points can only be created or annihilated in pairs of opposite chirality.

It was recently shown [2] that Weyl nodes come in two types. Type - I Weyl fermions have a point-like Fermi surface. When a magnetic field is applied, they exhibit a chiral Landau level [3–5] regardless of the magnetic field direction. When this chiral Landau level crosses the Fermi level, it can be a source of reduced magnetoresistance [6–11]. Type - II Weyl fermions on the other hand have an energy spectrum that is tilted by having a strong  $\sigma_0$  contribution to the Hamiltonian (eq. (1)). As a consequence, the Fermi surface becomes open and the chiral anomaly is anisotropic, appearing only for certain magnetic field directions.

Inversion symmetry  $P$  maps a Weyl node at point  $\mathbf{k}$  onto a Weyl node of opposite chirality at  $-\mathbf{k}$ . Similarly, time-reversal symmetry  $\mathcal{T}$  maps a Weyl point at  $\mathbf{k}$  onto one at  $-\mathbf{k}$ , but without changing its chirality. Consequently, in the presence of the product symmetry  $\mathcal{T} * P$ , Weyl nodes are mapped into themselves but with opposite chirality. This four-fold degenerate crossing, consisting of two superimposed Weyl points of opposite chirality, is known as a Dirac node. Unlike Weyl points, they are not protected from gapping by any quantized topological charge. Consequently, additional symmetries are needed to stabilize Dirac nodes.

In centrosymmetric non-magnetic materials, the presence of both inversion and time-reversal symmetry allows only for Dirac nodes to form. Weyl nodes are not possible unless the product symmetry  $\mathcal{T} * P$  is broken.

Recently, transition metal dipnictides of the type AB<sub>2</sub> ( $A \in \{\text{Ta}, \text{Nb}\}$ ,  $B \in \{\text{As}, \text{Sb}\}$ ) have gained a lot of attention [12–19] for their giant magnetoresistance. These materials are semimetals, but without a direct closure of the band gap. Consequently, they do not host any Weyl or Dirac points.

The exact nature of magnetoresistance in these materials - especially the dependency on the direction of the magnetic field - is still under active investigation. Negative magnetoresistance has been observed experimentally for NbAs<sub>2</sub> [17, 18], TaAs<sub>2</sub> [17] and TaSb<sub>2</sub> [17, 20]. Anomalous - albeit not negative - magnetoresistance has been observed for NbSb<sub>2</sub> [12] and TaAs<sub>2</sub> [15]. However, there are also experiments which point to the contrary, which is that there is no negative magnetoresistance in these materials. In Ref. [16], negative magnetoresistance was observed at first but then determined to be an artifact of the measurement setup.

In the following, we propose a mechanism for Weyl nodes to appear in these materials under the influence of a magnetic field. The chiral anomaly associated with these Weyl nodes is a possible source of negative magnetoresistance. Such an appearance of Weyl points under magnetic field has recently been proposed in Ref. [21]. The mechanism with which the Weyl points appear, however, is a different one - in this work the Weyl points appear from a previously gapped state, while the Ref. [21] discusses Weyl points arising from the splitting of a four-fold crossing.

The paper is structured as follows: In the first section, the atomic and electronic structure of the four compounds is described. A four-band Hamiltonian for TaAs<sub>2</sub> is derived from symmetry considerations and fitted to the band structure. In the second section, the topology of the band structure is studied, first without magnetic field and then by applying a Zeeman term. We find that this leads to the appearance of Weyl points.

## II. ATOMIC AND ELECTRONIC STRUCTURE OF AB<sub>2</sub> COMPOUNDS

### A. Atomic structure

In the following, the atomic structure of TaAs<sub>2</sub> [22], TaSb<sub>2</sub> [23], NbSb<sub>2</sub> [24] and NbAs<sub>2</sub> [25] is described.

The reduced unit cell of AB<sub>2</sub> compounds has the general form

$$\begin{aligned} a_1 &= (a, b, 0) \\ a_2 &= (-a, b, 0) \\ a_3 &= (-c, 0, d) \end{aligned} \quad (2)$$

with parameters as given in table I [22, 24].

	a	b	c	d
<b>TaAs<sub>2</sub></b>	4.6655	1.6915	3.8420	6.7330
<b>TaSb<sub>2</sub></b>	5.11	1.822	4.1950	7.1502
<b>NbAs<sub>2</sub></b>	4.684	1.698	3.8309	6.7933
<b>NbSb<sub>2</sub></b>	5.1198	1.8159	4.1705	7.2134

TABLE I. Unit cell dimensions (in Å) for AB<sub>2</sub> compounds.

Each unit cell contains 2 formula units. The atoms are located at general Wyckoff positions  $(x, -x, y)$ ,  $(-x, x, -y)$ , for  $(x, y)$  as shown in table II [22, 24].

Figure 1 shows the reduced unit cell and 1. BZ of TaAs<sub>2</sub>. The k-point path along which bandstructure calculations are performed is indicated. In the basis reciprocal to that of eq. (2), the special k-points are given by

$$\begin{aligned} \Gamma &= (0, 0, 0) \\ A &= (0, 0, 0.5) \\ L &= (0.5, 0, 0.5) \\ M &= (0.5, 0.5, 0.5) \\ V &= (0.5, 0, 0) \\ Y &= (0.5, 0.5, 0). \end{aligned} \quad (3)$$

	A	B1	B2
<b>TaAs<sub>2</sub></b>	(0.157, 0.1959)	(0.4054, 0.1082)	(0.1389, 0.5265)
<b>TaSb<sub>2</sub></b>	(0.152, 0.19)	(0.405, 0.113)	(0.147, 0.535)
<b>NbAs<sub>2</sub></b>	(0.1574, 0.1965)	(0.4059, 0.1084)	(0.14, 0.528)
<b>NbSb<sub>2</sub></b>	(0.1521, 0.1903)	(0.4051, 0.1127)	(0.1475, 0.5346)

TABLE II. Atomic positions  $(x, y)$ .

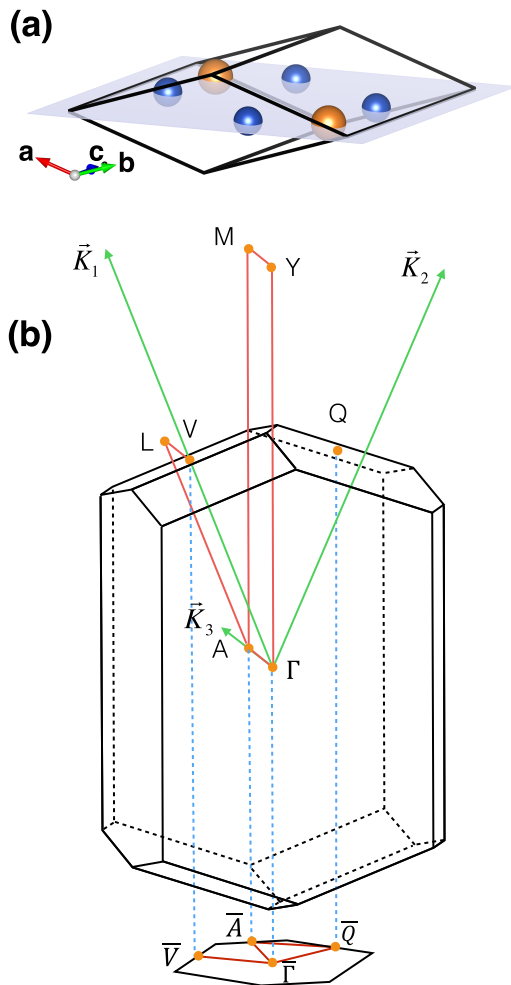


FIG. 1. (a) Reduced unit cell of TaAs<sub>2</sub>. (b) First BZ of TaAs<sub>2</sub>. The k-point path and its projection onto the 010 surface are indicated.

### B. Electronic structure

Electronic structure calculations were performed in VASP [26], with projector augmented-wave (PAW) [27, 28] pseudopotentials. The PBE approximation [29] was used, and spin-orbit coupling was included in the potentials. The self-consistent field (SCF) calculations were performed on a  $11 \times 11 \times 5$   $\Gamma$ -centered grid for TaAs<sub>2</sub>, and a  $10 \times 10 \times 5$   $\Gamma$ -centered grid for NbSb<sub>2</sub>. The energy cutoff given in the potential files was used, which is 293.2 eV for NbAs<sub>2</sub> and NbSb<sub>2</sub>, and 223.7 eV for TaAs<sub>2</sub> and TaSb<sub>2</sub>.

Additionally, the PBE calculations were tested against the accurate HSE06 hybrid functional [30, 31]. The hybrid SCF calculations for the band structures were performed on a  $\Gamma$ -centered  $6 \times 6 \times 4$  grid for all materials. For the generation of the Wannier tight-binding model of NbSb<sub>2</sub> a  $\Gamma$ -centered  $10 \times 10 \times 5$  grid was used.

The band structure of TaAs<sub>2</sub> and NbSb<sub>2</sub> is shown in fig. 2. Both materials exhibit a pair of electron and hole

pockets near the  $M$  - point, where the minimum band gap is about 318 meV (120 meV without hybrid functionals) in the case of TaAs<sub>2</sub>, 151 meV (98 meV) for TaSb<sub>2</sub>, 261 meV (22 meV) for NbAs<sub>2</sub>, and 67 meV (18 meV) in the case of NbSb<sub>2</sub>. A more complete calculation of the band structure can be found for example in Ref. [32].

### C. Symmetry operations and $\mathbf{k} \cdot \mathbf{p}$ model

The AB<sub>2</sub> compounds studied here have  $C2/m$  symmetry (space group 12). The rotation axis is along the cartesian  $y$ -axis. In reduced coordinates, the symmetry matrices are as follows:

- Identity  $E = \mathbb{I}_{3 \times 3}$
- Rotation  $C_{2y} = \begin{pmatrix} 0 & 1 & 0 \\ 1 & 0 & 0 \\ 0 & 0 & -1 \end{pmatrix}$
- Parity  $P = -\mathbb{I}_{3 \times 3}$
- Mirror  $M_y = PC_{2y} = \begin{pmatrix} 0 & -1 & 0 \\ -1 & 0 & 0 \\ 0 & 0 & 1 \end{pmatrix}$

	$E$	$C_{2y}$	$P$	$M_y$
$\Gamma_3^+$	1	$i$	1	$i$
$\Gamma_4^+$	1	$-i$	1	$-i$
$\Gamma_3^-$	1	$i$	-1	$-i$
$\Gamma_4^-$	1	$-i$	-1	$i$

TABLE III. Character table for the relevant double group representations of  $C_{2m}$  [33].

From the first-principles wave-functions, the representations corresponding to the two highest valence and two lowest conduction bands at the  $M$  - point were determined using the WIEN2k code [34, 35]. They were found to be  $\Gamma_3^+, \Gamma_4^+$  and  $\Gamma_3^-, \Gamma_4^-$ , respectively. Their characters are shown in table III, which comes from table 15 on page 35 in Koster et al. [33]. Consequently, the symmetry rep-

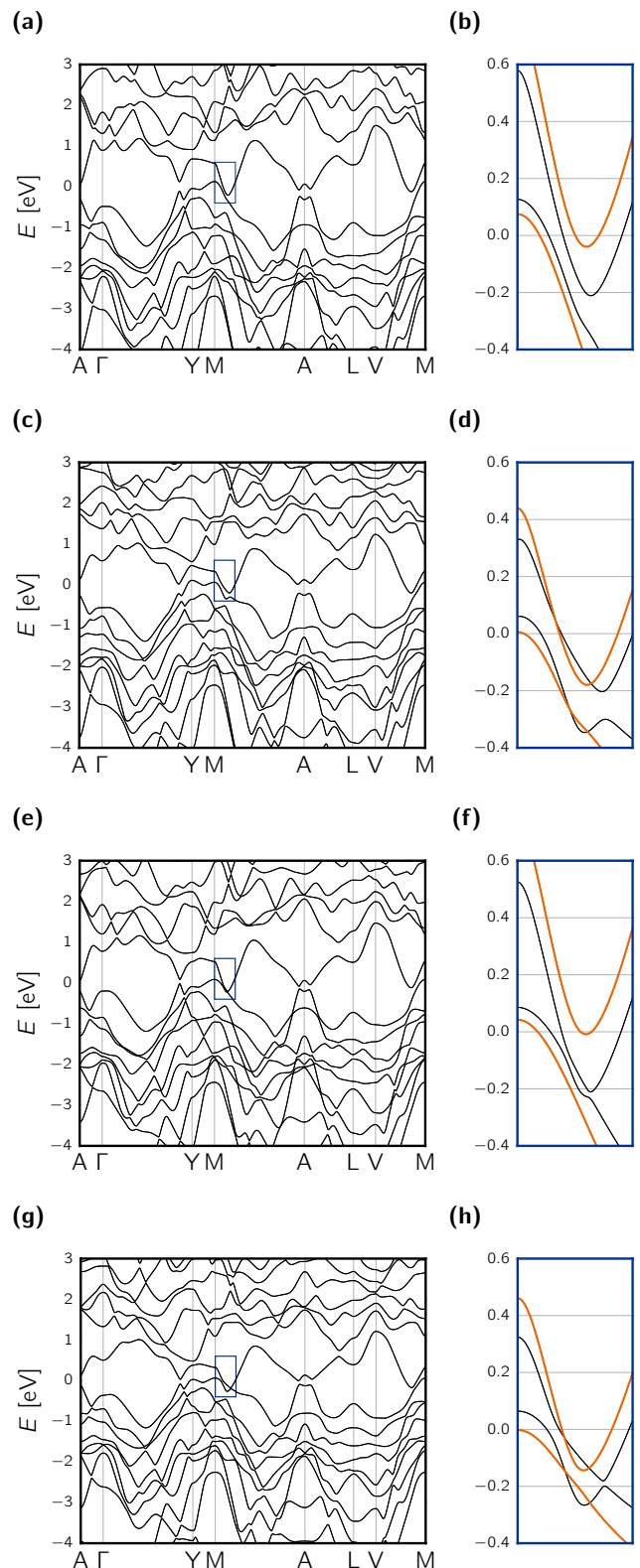


FIG. 2. Band structures of AB<sub>2</sub> compounds. The inset shows electron and hole pockets around  $M$ . The orange line represents calculations using hybrid functionals. (a-b) TaAs<sub>2</sub> (c-d) TaSb<sub>2</sub> (e-f) NbAs<sub>2</sub> (g-h) NbSb<sub>2</sub>

representations in these four bands are given by

- Identity  $E = \mathbb{I}_{4 \times 4}$
- Rotation  $C_{2y} = \begin{pmatrix} i & 0 & 0 & 0 \\ 0 & -i & 0 & 0 \\ 0 & 0 & i & 0 \\ 0 & 0 & 0 & -i \end{pmatrix}$
- Parity  $P = \begin{pmatrix} 1 & 0 & 0 & 0 \\ 0 & 1 & 0 & 0 \\ 0 & 0 & -1 & 0 \\ 0 & 0 & 0 & -1 \end{pmatrix}$
- Mirror  $M_y = PC_{2y} = \begin{pmatrix} i & 0 & 0 & 0 \\ 0 & -i & 0 & 0 \\ 0 & 0 & -i & 0 \\ 0 & 0 & 0 & i \end{pmatrix}$
- Time-reversal  $\mathcal{T} = \begin{pmatrix} 0 & -1 & 0 & 0 \\ 1 & 0 & 0 & 0 \\ 0 & 0 & 0 & -1 \\ 0 & 0 & 1 & 0 \end{pmatrix} \hat{K}$

For each of the symmetry operations  $g$ , the constraint

$$\mathcal{H}(\mathbf{k}) = D(g)\mathcal{H}(g^{-1}\mathbf{k})D(g^{-1}) \quad (4)$$

is imposed on the  $4 \times 4$  Hamiltonian, where  $D(g)$  is the symmetry representation. By applying these constraints on the general form of a four-band Hamiltonian

$$\mathcal{H}(\mathbf{k}) = \sum_{i,j \in \{0,x,y,z\}} C_{ij}(\mathbf{k})(\sigma_i \otimes \sigma_j), \quad (5)$$

we find the Hamiltonian to be of the form

$$\begin{aligned} \mathcal{H}(\mathbf{k}) = & C_{00}(\mathbf{k})(\sigma_0 \otimes \sigma_0) + C_{xx}(\mathbf{k})(\sigma_x \otimes \sigma_x) + \\ & C_{xy}(\mathbf{k})(\sigma_x \otimes \sigma_y) + C_{xz}(\mathbf{k})(\sigma_x \otimes \sigma_z) + \\ & C_{y0}(\mathbf{k})(\sigma_y \otimes \sigma_0) + C_{z0}(\mathbf{k})(\sigma_z \otimes \sigma_0), \end{aligned} \quad (6)$$

where the  $C_{ij}(\mathbf{k})$  are given up to second order in  $\mathbf{k}^* = \mathbf{k} - M$  (in reduced coordinates) by

$$\begin{aligned} C_{00}(\mathbf{k}^*) = & C_{00}^1 + C_{00}^{x^2+y^2}((k_x^*)^2 + (k_y^*)^2) + \\ & C_{00}^{xy} k_x^* k_y^* + C_{00}^{xz-yz}(k_x^* k_z^* - k_y^* k_z^*) + \\ & C_{00}^{z^2} (k_z^*)^2 \end{aligned} \quad (7)$$

$$\begin{aligned} C_{z0}(\mathbf{k}^*) = & C_{z0}^1 + C_{z0}^{x^2+y^2}((k_x^*)^2 + (k_y^*)^2) + \\ & C_{z0}^{xy} k_x^* k_y^* + C_{z0}^{xz-yz}(k_x^* k_z^* - k_y^* k_z^*) + \\ & C_{z0}^{z^2} (k_z^*)^2 \end{aligned} \quad (8)$$

$$C_{xx}(\mathbf{k}^*) = C_{xx}^{x-y}(k_x^* - k_y^*) + C_{xx}^z k_z^* \quad (9)$$

$$C_{xy}(\mathbf{k}^*) = C_{xy}^{x-y}(k_x^* - k_y^*) + C_{xy}^z k_z^* \quad (10)$$

$$C_{xz}(\mathbf{k}^*) = C_{xz}^{x+y}(k_x^* + k_y^*) \quad (11)$$

$$C_{y0}(\mathbf{k}^*) = C_{y0}^{x+y}(k_x^* + k_y^*). \quad (12)$$

These 16 parameters were numerically fitted to the band structure of TaAs<sub>2</sub> using the `scipy` [36] package, to

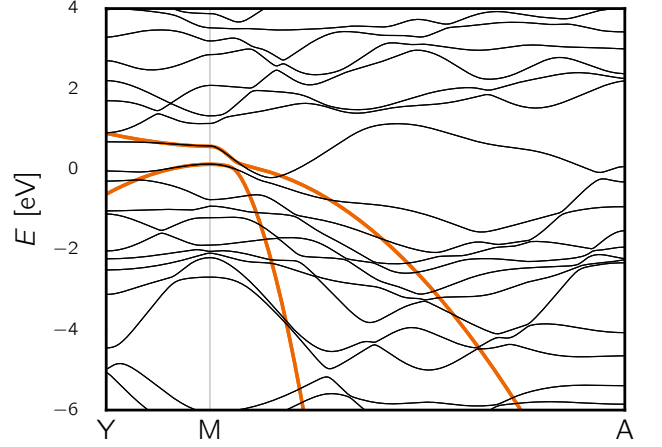


FIG. 3. TaAs<sub>2</sub> band structure of the  $\mathbf{k} \cdot \mathbf{p}$  model (thick orange line), compared to the first-principles result (black lines).

obtain the values in table IV. The resulting band structure around the  $M$ -point is shown in fig. 3. Comparing it to the band structure obtained from first-principles reveals that the approximation is accurate in the immediate vicinity of the  $M$ -point, but breaks down at around 6% of the distance along the line  $M - A$ . Importantly, the minimum band gap is not preserved in this model. Nevertheless, the model can be used to qualitatively study effects in TaAs<sub>2</sub>, owing to the fact that it contains the correct symmetry representations.

[eV]	$C_{00}^1 = 7.066$	$C_{z0}^1 = -0.224$
[eVÅ]	$C_{xz}^{x+y} = 1.272$	$C_{y0}^{x+y} = 1.270$
	$C_{xx}^{x-y} = -0.061$	$C_{xy}^{x-y} = -1.999$
	$C_{xx}^z = -0.554$	$C_{xy}^z = -0.253$
[eVÅ <sup>2</sup> ]	$C_{00}^{x^2+y^2} = -71.21$	$C_{z0}^{x^2+y^2} = 56.30$
	$C_{00}^{xy} = -137.1$	$C_{z0}^{xy} = 123.1$
	$C_{00}^{xz-yz} = 1.52$	$C_{z0}^{xz-yz} = -1.49$
	$C_{00}^{z^2} = -0.84$	$C_{z0}^{z^2} = -1.88$

TABLE IV. Parameters of the  $4 \times 4$  Hamiltonian of TaAs<sub>2</sub> around  $M$  up to second order.

### III. BAND STRUCTURE TOPOLOGY

In this section, we describe the band structure topology and the influence of magnetic field. First, we describe the topology in the absence of magnetic field for all four compounds. Then, we show that Weyl points appear under sufficient magnetic field. This result is shown first for the  $\mathbf{k} \cdot \mathbf{p}$  model of TaAs<sub>2</sub> derived in section II C, and then for a tight-binding model of NbSb<sub>2</sub> derived from first-principles.

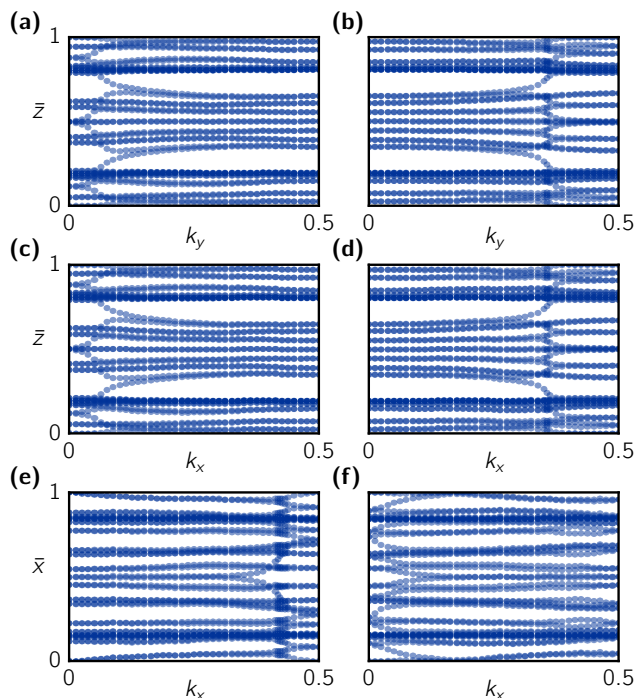


FIG. 4. Wannier charge center evolution for the time-reversal invariant planes of TaAs<sub>2</sub>. (a)  $k_x = 0$  (b)  $k_x = 0.5$  (c)  $k_y = 0$  (d)  $k_y = 0.5$  (e)  $k_z = 0$  (f)  $k_z = 0.5$

### A. Band structure topology without magnetic fields

In the absence of magnetic field, there is no direct band gap closure in AB<sub>2</sub> compounds. Since the valence bands thus form a well-defined manifold, they can be classified, just like insulators, according to the topology of these valence bands. Because time-reversal symmetry is fulfilled, a  $\mathbb{Z}_2$  classification is possible.

All compounds were found to be weak topological insulators, with  $\mathbb{Z}_2$  indices 0; (111). That is, all time-reversal invariant planes  $k_i = 0, 0.5$  have a non-trivial  $\mathbb{Z}_2$  index  $\Delta = 1$ . This result was derived from first-principles using the Z2Pack code [37], and agrees with previous studies [15, 17, 32]. The corresponding evolution of Wannier charge centers is shown, for the case of TaAs<sub>2</sub>, in fig. 4.

Figure 5 shows the surface density of states for a slab of TaAs<sub>2</sub>, with surfaces parallel to the mirror plane perpendicular to the cartesian  $y$ -axis (the light blue plane shown in fig. 1). The presence of topological surface states confirms the conclusion that the material is a weak topological insulator. The surface spectrum was calculated by the iterative Green's function [38] which was implemented in WannierTools [39].

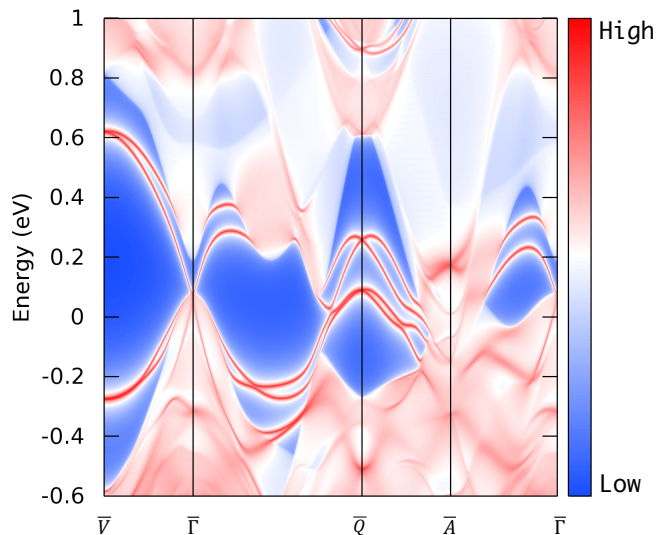


FIG. 5. Surface density of states of TaAs<sub>2</sub> on the 010 surface, along the  $k$ -point path shown in fig. 1.

### B. Effect of Zeeman splitting on the $\mathbf{k} \cdot \mathbf{p}$ model for TaAs<sub>2</sub>

Here we study the effects of magnetic field on TaAs<sub>2</sub> by adding a Zeeman splitting term to the  $\mathbf{k} \cdot \mathbf{p}$  model derived in section II C (eq. (6)). The splitting term is given by

$$\Delta\mathcal{H} = c_x\sigma_0 \otimes \sigma_y + c_y\sigma_0 \otimes \sigma_z + c_z\sigma_0 \otimes \sigma_x, \quad (13)$$

where  $c_i$  is the strength of the Zeeman splitting induced by the magnetic field in that direction, that is

$$c_i = \sum_j g_{ij}\mu_B H_j. \quad (14)$$

This assumes that the  $g$ -factor is equal for all bands. The limitations of this approximation are discussed in section III D.

#### 1. Magnetic field along the rotation axis $\hat{y}$

When magnetic field is applied along the rotation axis  $\hat{y}$ , the Zeeman term (eq. (13)) takes the form

$$\Delta\mathcal{H} = c_y\sigma_0 \otimes \sigma_z. \quad (15)$$

This term preserves all spatial symmetries of the system, breaking only time-reversal.

Along the  $M - A$  line, the  $C_{xx}$  and  $C_{yy}$  contributions to the Hamiltonian vanish since  $k_x^* = k_y^*$  and  $k_z^* = 0$ . Consequently, the energy eigenvalues are given by

$$E(\mathbf{k}) = C_{00}(\mathbf{k}) \pm c_y \mp \sqrt{C_{xz}(\mathbf{k})^2 + C_{y0}(\mathbf{k})^2 + C_{z0}(\mathbf{k})^2} \quad (16)$$

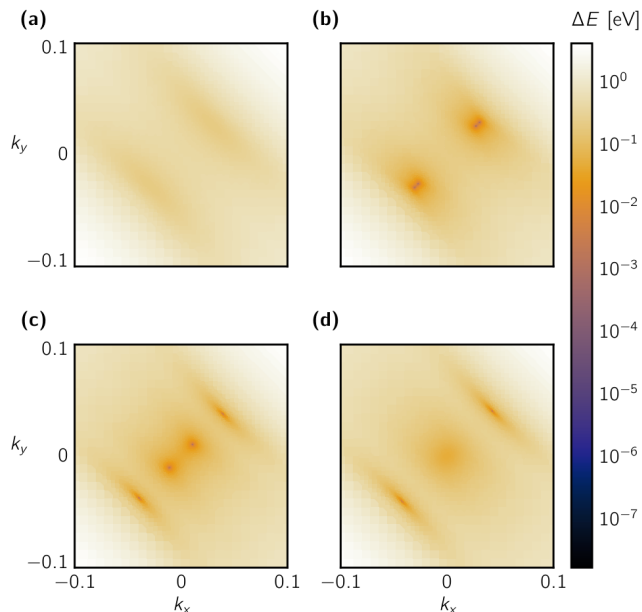


FIG. 6. Band gap of TaAs<sub>2</sub> in the  $k_z^* = 0$  plane for different values of the magnetic field in  $y$ -direction, calculated from the  $\mathbf{k} \cdot \mathbf{p}$  model. A dark spot indicates the presence of a Weyl point. (a) No magnetic field. There are no Weyl points present (b)  $c_y = 0.11$  eV. Two pairs of Weyl points have appeared on the  $k_x = k_y$  line. (c)  $c_y = 0.2$  eV. The pair of Weyl points move further apart. (d)  $c_y = 0.25$  eV. One pair of Weyl points has annihilated at  $M$ , leaving two Weyl points.

The Zeeman term counteracts the original splitting (square root term), such that for sufficient magnetic field there will be a direct band gap closure. Away from the  $M - A$  line, the band gap remains open, giving rise to a Weyl point.

When the Zeeman splitting is gradually switched on, two pairs of Weyl points form at about  $c_y = 0.11$  eV. Increasing the Zeeman splitting leads to a separation between the two nodes in a pair, with one node each moving towards the  $M$ -point. Finally, at  $c_y \approx 0.25$  eV, these two nodes meet at  $M$  and annihilate. This process is shown in fig. 6.

The existence of these Weyl points was confirmed by verifying that the nodes are a source or sink of Berry curvature. For this purpose, the Chern number of spheres surrounding the points was calculated by tracking hybrid Wannier charge centers (HWCC) on loops around the sphere [2, 37, 40, 41], using the Z2Pack software [37]. Figure 7 shows the evolution of the sum of HWCC for two of four nodes found at  $c_y = 0.12$  eV, demonstrating that the two points are Weyl nodes of opposite chirality.

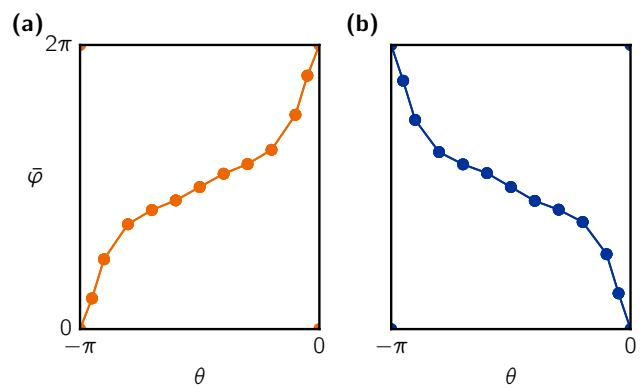


FIG. 7. Evolution of the sum of HWCC on spheres surrounding the Weyl points at  $c_y = 0.12$  eV splitting. (a) Weyl point at  $\mathbf{k} = (0.5247, 0.5247, 0.5)$ , having positive chirality  $C = +1$  (b) Weyl point at  $\mathbf{k} = (0.53258, 0.53258, 0.5)$  with negative chirality  $C = -1$

## 2. General magnetic field direction

Finally, the effects of a magnetic field in a general direction were studied. It turns out that, even though such a field breaks the spatial symmetries of the system, Weyl nodes still appear under a strong enough magnetic field. When magnetic field is applied in  $\hat{x}$  or  $\hat{z}$  - direction, a single pair of Weyl points emerges from the  $M$  point. These Weyl nodes are located on the  $k_x = -k_y$  plane, as shown in table V.

Splitting [eV]	Weyl position $\mathbf{k}^*$	Chirality
$c_x = 0.225$	$(-0.0042, 0.0042, 0.00093)$	-1
	$(0.0042, -0.0042, -0.00093)$	1
$c_x = 0.25$	$(-0.025, 0.025, 0.0054)$	-1
	$(0.025, -0.025, -0.0054)$	1
$c_x = 0.3$	$(-0.044, 0.044, 0.0098)$	-1
	$(0.044, -0.044, -0.0098)$	1
$c_z = 0.225$	$(0.0011, -0.0011, -0.018)$	-1
	$(-0.0011, 0.0011, 0.018)$	1
$c_z = 0.25$	$(0.0066, -0.0066, -0.11)$	-1
	$(-0.0066, 0.0066, 0.11)$	1
$c_z = 0.3$	$(0.012, -0.012, -0.18)$	-1
	$(-0.012, 0.012, 0.18)$	1

TABLE V. Position  $\mathbf{k}^* = \mathbf{k} - M$  (in reduced coordinates) and chirality of Weyl points for Zeeman splittings in  $\hat{x}$  and  $\hat{z}$ -direction.

Figure 8 shows the number of Weyl points as a function of the Zeeman splitting. To obtain this phase diagram, candidate Weyl points were identified using a

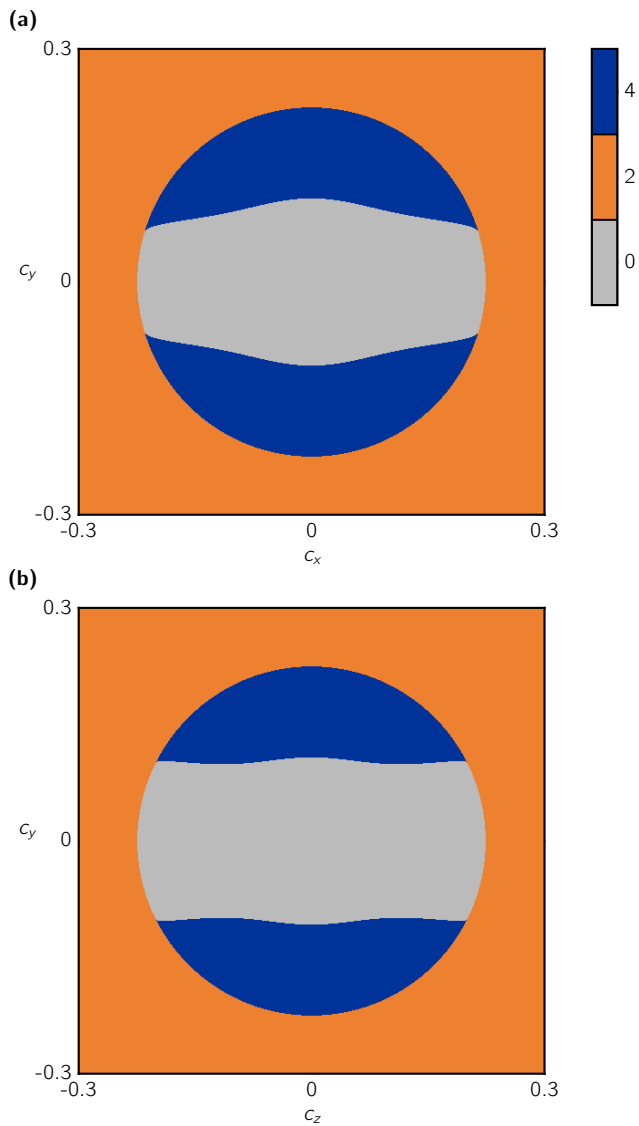


FIG. 8. Phase diagram showing the number of Weyl points in the  $\mathbf{k} \cdot \mathbf{p}$  model of TaAs<sub>2</sub> as a function of the Zeeman splitting (in eV).

quasi Newton algorithm to find minima in the band gap (using `scipy.optimize.minimize` [36]), for different initial guesses. In a second step, the Chern number on a small sphere (radius  $10^{-4} \text{ \AA}^{-1}$ ) surrounding the candidate points was evaluated (using Z2Pack [37]), keeping only points with a non-zero Chern number. Finally, duplicate points were eliminated by checking whether two points lie within the diameter of the sphere of one another.

### C. Effect of Zeeman splitting on the tight-binding model for NbSb<sub>2</sub>

Having studied the effects of Zeeman splitting on the  $\mathbf{k} \cdot \mathbf{p}$  model for TaAs<sub>2</sub>, we now study a more realistic tight-binding model for NbSb<sub>2</sub>, derived from a first-principles calculation with hybrid functionals using the Wannier90 code [42, 43]. NbSb<sub>2</sub> was chosen because it has the smallest direct band gap of the four materials, making it the most promising candidate for hosting Weyl points at realistic magnetic field strength.

The Zeeman splitting for this model can again be expressed by adding the corresponding terms to the Hamiltonian

$$\Delta\mathcal{H} = c_x\sigma_x \otimes \mathbb{I}_{22 \times 22} + c_y\sigma_y \otimes \mathbb{I}_{22 \times 22} + c_z\sigma_z \otimes \mathbb{I}_{22 \times 22}, \quad (17)$$

where the change in the splitting terms (compared to eq. (13)) is due to the different orbital basis used for the tight-binding model. We search for Weyl points between the last valence band and the first conduction band.

First we study the effect of applying a magnetic field in the  $y$ -direction. Figure 9 shows the effect of this splitting along the  $M - A$  line. For  $c_y \approx 0.06$  eV, two pairs of Weyl points appear close to the  $M - A$  line. The reason these points are not exactly on the line is because the crystal symmetry is broken when constructing the Wannier-based tight-binding model [42, 43]. Apart from this numerical difference, this effect is analogous to the case of the  $\mathbf{k} \cdot \mathbf{p}$  model for TaAs<sub>2</sub>, where the two pairs of Weyl points appeared at  $c_y = 0.11$  eV.

Table VI shows the Weyl point positions, chirality and type for selected values of the Zeeman splitting. It shows that Weyl points appear even at smaller values of  $c_y$  away from the  $M - A$  line. This is a crucial difference to the  $\mathbf{k} \cdot \mathbf{p}$  model which is valid only near the  $M$  point. Furthermore, all Weyl points found for these splitting values are of type II [2]. Type - II Weyl points have a tilted energy spectrum, making their Fermi surface open instead of point-like. As a consequence, their chiral anomaly – and their effect on magnetoresistance – is expected to be anisotropic.

Finally, a phase diagram showing the number of Weyl points as a function of magnetic field was calculated (see fig. 10). Unlike for the  $\mathbf{k} \cdot \mathbf{p}$  model, the number of Weyl points keeps increasing when the applied Zeeman term grows stronger. Again, the reason for this difference is that Weyl points also form far away from the  $M$  point, where the  $\mathbf{k} \cdot \mathbf{p}$  approximation is no longer applicable.

For some values of the splitting, the phase diagram shows an odd number of Weyl points, which is physically impossible. The reason for this is that the numerical procedure used to identify the number of Weyl points may not find a Weyl point if it is too close to another Weyl point. Since this problem occurs only rarely (see fig. 11), the phase diagram is still valid overall. Also, the procedure ensures that no Weyl point can be counted twice, so the phase diagram represents a lower limit for the real number of Weyl points. Thus, the general result

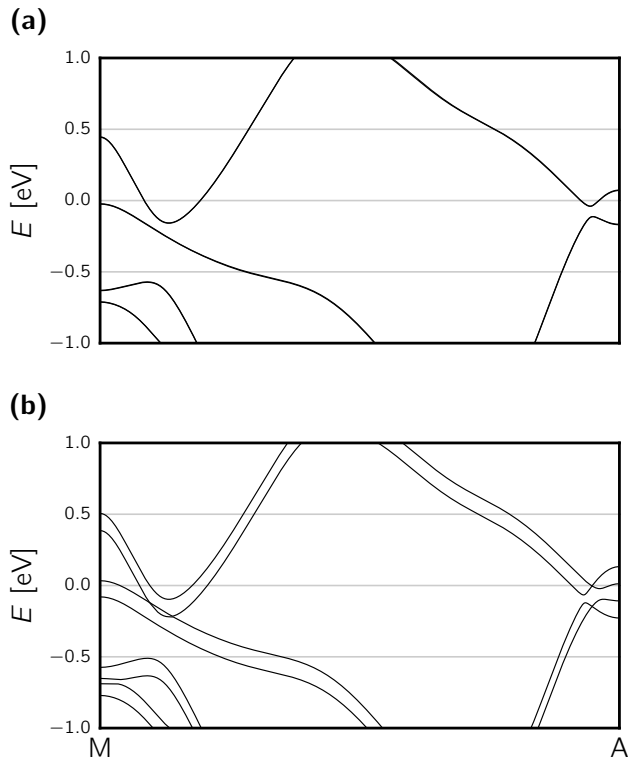


FIG. 9. Band structure of the tight-binding model for NbSb<sub>2</sub> along the  $M - A$  line. (a) Without Zeeman splitting. (b) With  $c_y = 0.06$  eV Zeeman splitting.

that the number of Weyl points increases with stronger Zeeman splitting remains valid.

#### D. Limitations of the model for magnetic field

In the previous sections the effect of magnetic field was modeled by applying a Zeeman splitting to the model Hamiltonian. The discussion was simplified by assuming that the  $g$ -factor is equal for all energy bands, and independent of  $\mathbf{k}$ . Here we discuss how the results might change if this assumption is not made.

If the  $g$ -factor is  $k$ -dependent, but still the same for all energy bands, the results above will change quantitatively, but not qualitatively. The reason for this is that a Weyl node that appears at a specific  $k$ -point will still be there, but for a different magnetic field. That is, the order in which the Weyl nodes at different  $k$ -points appear might change, but not the overall picture that there is an increasing number of Weyl points with stronger magnetic field.

The same is true if the  $g$ -factor varies for different energy bands, as long as the sign of the  $g$ -factor remains the same. Because the appearance of Weyl points is due to the relative Zeeman splitting between the last valence and first electron bands, it does not matter how much the splitting on each band contributes.

Split. [eV]	Position $\mathbf{k}$	Chir.	Type
$c_x = 0.045$	(0.4393, 0.4460, 0.5004)	+1	II
	(0.4359, 0.4444, 0.5026)	-1	II
	(0.5641, 0.5556, 0.4974)	+1	II
	(0.5607, 0.5540, 0.4996)	-1	II
$c_y = 0.03$	(0.3670, 0.5141, 0.0977)	+1	II
	(0.3655, 0.5142, 0.1004)	-1	II
	(0.6345, 0.4858, 0.8997)	+1	II
	(0.6330, 0.4858, 0.9023)	-1	II
$c_y = 0.04$	(0.3724, 0.5116, 0.0890)	+1	II
	(0.3627, 0.5135, 0.1055)	-1	II
	(0.6373, 0.4865, 0.8945)	+1	II
	(0.6276, 0.4884, 0.9110)	-1	II
	(0.9028, 0.0340, 0.5451)	+1	II
	(0.9018, 0.0354, 0.5390)	-1	II
	(0.0982, 0.9646, 0.4610)	+1	II
	(0.0974, 0.9658, 0.4545)	-1	II
$c_y = 0.06$	(0.3791, 0.5068, 0.0775)	+1	II
	(0.3592, 0.5131, 0.1108)	-1	II
	(0.6407, 0.4869, 0.8892)	+1	II
	(0.6211, 0.4929, 0.9222)	-1	II
	(0.9033, 0.0328, 0.5532)	+1	II
	(0.9006, 0.0364, 0.5314)	-1	II
	(0.0994, 0.9636, 0.4686)	+1	II
	(0.0968, 0.9671, 0.4467)	-1	II
	(0.4493, 0.4555, 0.5031)	+1	II
	(0.4309, 0.4320, 0.4825)	-1	II
$c_z = 0.0475$	(0.4494, 0.4384, 0.4853)	+1	II
	(0.4420, 0.4366, 0.4816)	-1	II
	(0.5580, 0.5634, 0.5184)	+1	II
	(0.5506, 0.5616, 0.5147)	-1	II

TABLE VI. Weyl point positions (in reduced coordinates), chirality and type for different values of the Zeeman splitting in the tight-binding model for NbSb<sub>2</sub>.

If the  $g$ -factors in the relevant bands have opposite sign however, there is a qualitative change in the behavior. This is illustrated in the following with the example of the  $\mathbf{k} \cdot \mathbf{p}$  model of TaAs<sub>2</sub> discussed in sections II C and III B. To account for the opposite sign of the  $g$ -factor for valence and conduction bands, the Zeeman splitting term (eq. (13)) is changed to

$$\Delta\mathcal{H} = c_x\sigma_z \otimes \sigma_y + c_y\sigma_z \otimes \sigma_z + c_z\sigma_z \otimes \sigma_x. \quad (18)$$

With  $c_y$  splitting, the energy bands on the mirror plane

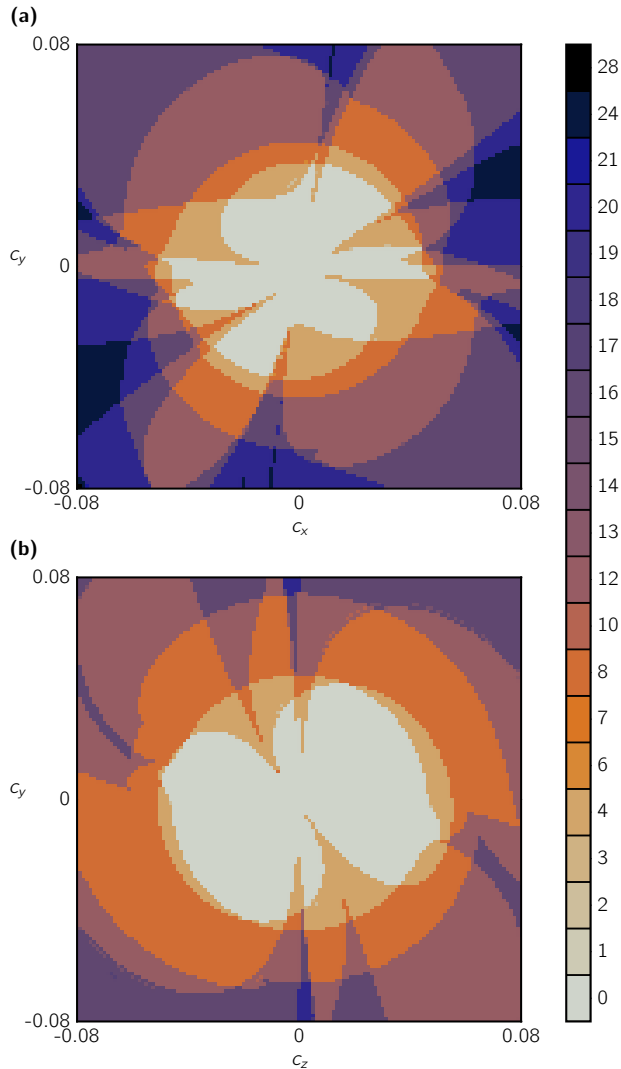


FIG. 10. Phase diagram showing the number of Weyl points as a function of Zeeman splitting (in eV) for the tight-binding model for NbSb<sub>2</sub>.

is then given by

$$E(\mathbf{k}) = C_{00}(\mathbf{k}) \pm c_y \mp \sqrt{C_{xx}(\mathbf{k})^2 + C_{xy}(\mathbf{k})^2 + C_{z0}(\mathbf{k})^2}. \quad (19)$$

As in eq. (16), the Zeeman term counteracts the original splitting. The difference to the previous case is that this equation holds on an entire plane in reciprocal space instead of just a line. As consequence, we can expect the appearance of a nodal line with sufficient Zeeman splitting. Indeed, a nodal line appears for  $c_y \gtrsim 0.2242$  eV, as shown in fig. 12. The Berry phase on a closed path around this nodal line was calculated to be  $\pi$ , using the Z2Pack [37] software. This verifies the topological nature of the nodal line.

In conclusion, the qualitative result obtained above remains intact when the g-factors are assumed to be

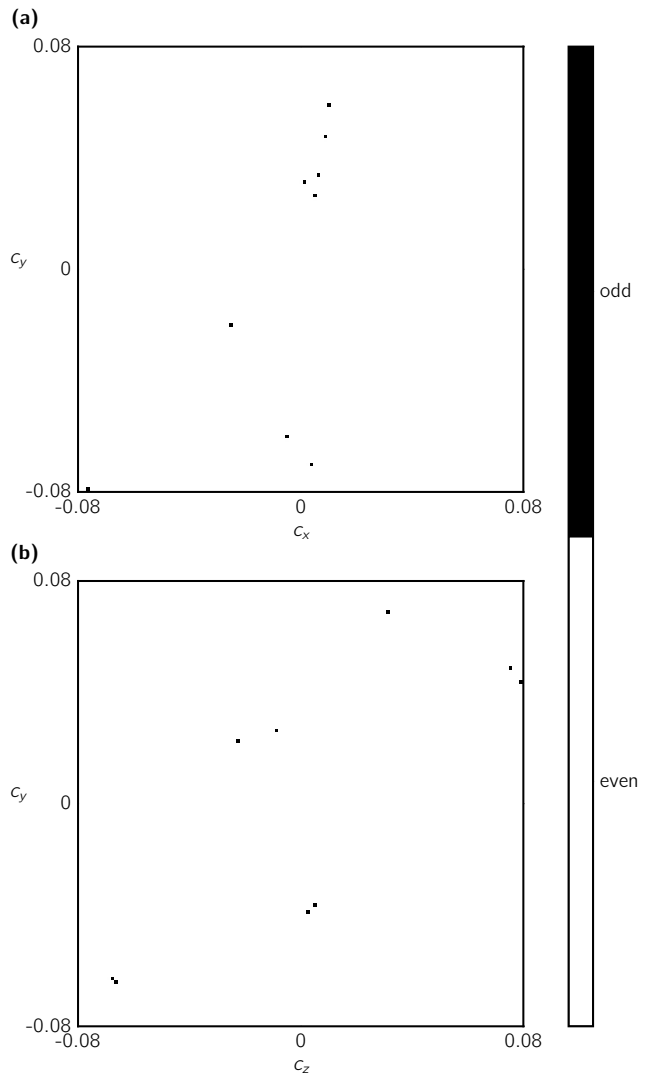


FIG. 11. Phase diagram showing whether the number of Weyl points shown in fig. 10 is even (physically possible) and odd (non-physical). The odd phases are a relict of the numerical evaluation of the phase.

$k$ -dependent and different for valence and conduction bands, as long as they keep the same sign. A more adequate model of the magnetic field is needed to establish the exact qualitative and quantitative nature of the topological phases with applied magnetic field. The current results indicate that Weyl nodes will appear at least for some directions of magnetic field.

#### IV. CONCLUSIONS

We studied the topological phase of transition metal dipnictides of the type AB<sub>2</sub> ( $A \in \{\text{Ta}, \text{Nb}\}$ ,  $B \in \{\text{As}, \text{Sb}\}$ ), with and without external magnetic field. In the absence of magnetic field, we found – in accordance with previous results [15, 17] – that these materials can be

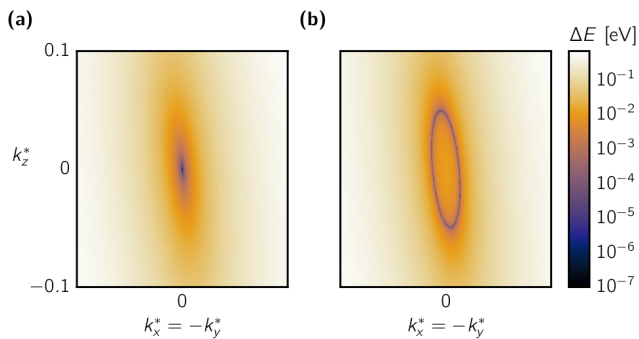


FIG. 12. Band gap of TaAs<sub>2</sub> on the mirror plane with Zeeman splitting as given in eq. (18). (a) At  $c_y \approx 0.2242$  eV, a nodal line appears at the  $M$ -point. (b) The nodal line expands for stronger splitting ( $c_y = 0.23$  eV).

classified as weak topological insulators despite having an indirect band gap closure.

The effect of a magnetic field was studied by applying a Zeeman splitting. We found that Weyl points can appear. We showed this result first from theoretical considerations on a four-band  $\mathbf{k} \cdot \mathbf{p}$  model, and numerically on a  $\mathbf{k} \cdot \mathbf{p}$  model of TaAs<sub>2</sub> and a tight-binding model of NbSb<sub>2</sub>. In the tight-binding model, we found the number of Weyl points to be increasing with growing magnetic field. For specific values of the Zeeman splitting, the type of the Weyl points in the tight-binding model was studied, and they were all found to be of type II.

The appearance of such field-induced Weyl points

could help explain the reduced or negative magnetoresistivity in these materials. However, it is unclear whether the Weyl points studied here appear at a magnetic field that is realistic to observe in experiments. Further studies, in particular to obtain a realistic  $g$ -factor and more reliable data for the direct band gap, are required to accurately estimate the required magnetic field. Furthermore, it is known that modeling a strong magnetic field with only Zeeman splitting is not sufficient, and a more accurate model should be considered. Finally, the effect of these Weyl points on the magnetoresistance should be calculated. This is influenced by the orientation of the type-II Weyl points, and their distance from the Fermi level.

Consequently, there are three open questions which require further investigation: First, whether the appearance of field-induced Weyl points is realistic in these AB<sub>2</sub> compounds. Second, if these Weyl points do appear, whether they alone are responsible for the experimentally observed behavior of magneto-resistance or if there are other effects. Finally, whether there are other compounds which contain the same kind of field-induced Weyl points, possibly appearing already at weaker magnetic field.

## V. ACKNOWLEDGMENTS

We would like to thank D. Rodic and M. Könz for helpful discussions. The authors were supported by Microsoft Research, and the Swiss National Science Foundation through the National Competence Centers in Research MARVEL and QSIT.

- 
- [1] GE Volovik, “Zeros in the Fermion spectrum in superfluid systems as diabolical points,” *JETP Lett* **46** (1987).
  - [2] Alexey A Soluyanov, Dominik Gresch, Zhijun Wang, QuanSheng Wu, Matthias Troyer, Xi Dai, and B Andrei Bernevig, “Type-II Weyl semimetals,” *Nature* **527**, 495–498 (2015).
  - [3] Stephen L. Adler, “Axial-vector vertex in spinor electrodynamics,” *Phys. Rev.* **177**, 2426–2438 (1969).
  - [4] John S Bell and Roman Jackiw, “A PCAC puzzle:  $\pi^0 \rightarrow \gamma\gamma$  in the  $\sigma$ -model,” *Il Nuovo Cimento A* **60**, 47–61 (1969).
  - [5] Holger Bech Nielsen and Masao Ninomiya, “The Adler-Bell-Jackiw anomaly and Weyl Fermions in a crystal,” *Phys. Lett. B* **130**, 389–396 (1983).
  - [6] AA Abrikosov, “Quantum magnetoresistance,” *Phys. Rev. B* **58**, 2788 (1998).
  - [7] DT Son and BZ Spivak, “Chiral anomaly and classical negative magnetoresistance of Weyl metals,” *Phys. Rev. B* **88**, 104412 (2013).
  - [8] Xiaochun Huang, Lingxiao Zhao, Yujia Long, Peipei Wang, Dong Chen, Zhanhai Yang, Hui Liang, Mianqi Xue, Hongming Weng, Zhong Fang, Xi Dai, and Genfu Chen, “Observation of the chiral-anomaly-induced negative magnetoresistance in 3D Weyl semimetal TaAs,” *Phys. Rev. X* **5**, 031023 (2015).
  - [9] Jun Xiong, Satya K Kushwaha, Tian Liang, Jason W Krizan, Max Hirschberger, Wudi Wang, RJ Cava, and NP Ong, “Evidence for the chiral anomaly in the Dirac semimetal Na<sub>3</sub>Bi,” *Science* **350**, 413–416 (2015).
  - [10] Frank Arnold, Chandra Shekhar, Shu-Chun Wu, Yan Sun, Ricardo Donizeth dos Reis, Nitesh Kumar, Marcel Naumann, Mukkattu O Ajeesh, Marcus Schmidt, Adolfo G Grushin, *et al.*, “Negative magnetoresistance without well-defined chirality in the Weyl semimetal TaP,” *Nature Comm.* **7** (2016).
  - [11] Xiaojun Yang, Yupeng Liu, Zhen Wang, Yi Zheng, and Zhu-an Xu, “Chiral anomaly induced negative magnetoresistance in topological Weyl semimetal NbAs,” (2015), [arXiv:1506.03190](https://arxiv.org/abs/1506.03190).
  - [12] Kefeng Wang, D Graf, Lijun Li, Limin Wang, and C Petrovic, “Anisotropic giant magnetoresistance in NbSb<sub>2</sub>,” *Scientific reports* **4** (2014).
  - [13] Yi-Yan Wang, Qiao-He Yu, Peng-Jie Guo, Kai Liu, and Tian-Long Xia, “Resistivity plateau and extremely large magnetoresistance in NbAs<sub>2</sub> and TaAs<sub>2</sub>,” *Phys. Rev. B* **94**, 041103 (2016).
  - [14] Desheng Wu, Jian Liao, Wei Yi, Xia Wang, Peigang Li, Hongming Weng, Youguo Shi, Yongqing Li, Jianlin Luo, Xi Dai, *et al.*, “Giant semiclassical magnetoresistance in high mobility TaAs<sub>2</sub> semimetal,” *Appl. Phys. Lett.* **108**,

- 042105 (2016).
- [15] Yongkang Luo, R. D. McDonald, P. F. S. Rosa, B. Scott, N. Wakeham, N. J. Ghimire, E. D. Bauer, J. D. Thompson, and F. Ronning, “Anomalous electronic structure and magnetoresistance in TaAs<sub>2</sub>,” *Scientific Reports* **6**, 27294 EP – (2016), article.
- [16] Zhujun Yuan, Hong Lu, Yongjie Liu, Junfeng Wang, and Shuang Jia, “Large magnetoresistance in compensated semimetals TaAs<sub>2</sub> and NbAs<sub>2</sub>,” *Phys. Rev. B* **93**, 184405 (2016).
- [17] Yupeng Li, Zhen Wang, Yunhao Lu, Xiaojun Yang, Zhixuan Shen, Feng Sheng, Chunmu Feng, Yi Zheng, and Zhu-An Xu, “Negative magnetoresistance in topological semimetals of transition-metal dipnictides with nontrivial  $\mathbb{Z}_2$  indices,” (2016), [arXiv:1603.04056](https://arxiv.org/abs/1603.04056).
- [18] Bing Shen, Xiaoyu Deng, Gabriel Kotliar, and Ni Ni, “Fermi surface topology and negative longitudinal magnetoresistance observed in the semimetal NbAs<sub>2</sub>,” *Phys. Rev. B* **93**, 195119 (2016).
- [19] Zheng Wang, Yupeng Li, Yunhao Lu, Zhixuan Shen, Feng Sheng, Chunmu Feng, Yi Zheng, and Zhuan Xu, “Topological phase transition induced extreme magnetoresistance in  $\text{tasb}_{-}\{2\}$ ,” arXiv preprint [arXiv:1603.01717](https://arxiv.org/abs/1603.01717) (2016).
- [20] Yuke Li, Lin Li, Jialu Wang, Tingting Wang, Xiaofeng Xu, Chuanying Xi, Chao Cao, and Jianhui Dai, “Resistivity plateau and negative magnetoresistance in the topological semimetal TaSb<sub>2</sub>,” *Phys. Rev. B* **94**, 121115 (2016).
- [21] Jennifer Cano, Barry Bradlyn, Zhijun Wang, Max Hirschberger, NP Ong, and BA Bernevig, “The chiral anomaly factory: Creating Weyls with a magnetic field,” (2016), [arXiv:1604.08601](https://arxiv.org/abs/1604.08601).
- [22] RG Ling and C Belin, “Affinement de la structure cristalline du diarseniure de tantale,” *CR Acad. Sci. Paris* **292**, 891–893 (1981).
- [23] F Hulliger, “New representatives of the NbAs<sub>2</sub> and ZrAs<sub>2</sub> structures,” (1964).
- [24] Ya F Lomnytska and VV Berezovets, “Phase relations in the Nb-Ni-Sb system,” *Inorganic materials* **41**, 1166–1171 (2005).
- [25] Wolfgang Bensch and Wolfram Heid, “NbAs<sub>2</sub>,” *Acta Crystallographica Section C: Crystal Structure Communications* **51**, 2205–2207 (1995).
- [26] Georg Kresse and Jürgen Furthmüller, “Efficiency of ab-initio total energy calculations for metals and semiconductors using a plane-wave basis set,” *Computational Materials Science* **6**, 15–50 (1996).
- [27] Peter E Blöchl, “Projector augmented-wave method,” *Phys. Rev. B* **50**, 17953 (1994).
- [28] Georg Kresse and D Joubert, “From ultrasoft pseudopotentials to the projector augmented-wave method,” *Phys. Rev. B* **59**, 1758 (1999).
- [29] John P Perdew, Kieron Burke, and Matthias Ernzerhof, “Generalized gradient approximation made simple,” *Phys. Rev. Lett.* **77**, 3865 (1996).
- [30] Jochen Heyd, Gustavo E. Scuseria, and Matthias Ernzerhof, “Hybrid functionals based on a screened Coulomb potential,” *J. Chem. Phys.* **118**, 8207–8215 (2003).
- [31] Aliaksandr V. Kruckau, Oleg A. Vydrov, Artur F. Izmaylov, and Gustavo E. Scuseria, “Influence of the exchange screening parameter on the performance of screened hybrid functionals,” *J. Chem. Phys.* **125**, 224106–224106 (2006).
- [32] Chenchao Xu, Jia Chen, Guo-Xiang Zhi, Yuke Li, Jianhui Dai, and Chao Cao, “Electronic structures of transition metal dipnictides XPn<sub>2</sub> (X = Ta, Nb; Pn = P, As, Sb),” *Phys. Rev. B* **93**, 195106 (2016).
- [33] G. F. Koster, J. O. Dimmock, R. G. Wheeler, and H. Statz, *Properties of the thirty-two point groups*, Vol. 24 (The MIT Press, 1963).
- [34] Peter Blaha, Karlheinz Schwarz, GKH Madsen, Dieter Kvasnicka, and Joachim Luitz, *WIEN2k* (Technical Universität Wien Austria, 2001).
- [35] Karlheinz Schwarz, Peter Blaha, and GKH Madsen, “Electronic structure calculations of solids using the WIEN2k package for material sciences,” *Computer Phys. Comm.* **147**, 71–76 (2002).
- [36] Eric Jones, Travis Oliphant, Pearu Peterson, *et al.*, “SciPy: Open source scientific tools for Python,” (2001–), [Online; accessed 2015-05-26].
- [37] Dominik Gresch, Gabriel Autès, Oleg V. Yazyev, Matthias Troyer, David Vanderbilt, B. Andrei Bernevig, and Alexey A. Soluyanov, “Z2Pack: Numerical implementation of hybrid Wannier centers for identifying topological materials,” (2016), [arXiv:1610.08983](https://arxiv.org/abs/1610.08983).
- [38] M P Lopez Sancho, J M Lopez Sancho, J M L Sancho, and J Rubio, “Highly convergent schemes for the calculation of bulk and surface green functions,” *Journal of Physics F: Metal Physics* **15**, 851 (1985).
- [39] Quan Sheng Wu and Sheng Nan Zhang, “Wannier Tools,” [https://github.com/quanshengwu/wannier\\_tools](https://github.com/quanshengwu/wannier_tools) (2015).
- [40] Zhijun Wang, Dominik Gresch, Alexey A Soluyanov, Weiwei Xie, S Kushwaha, Xi Dai, Matthias Troyer, Robert J Cava, and B Andrei Bernevig, “MoTe<sub>2</sub>: a type-II Weyl topological metal,” *Phys. Rev. Lett.* **117**, 056805 (2016).
- [41] Gabriel Autès, Dominik Gresch, Matthias Troyer, Alexey A. Soluyanov, and Oleg V. Yazyev, “Robust type-II Weyl semimetal phase in transition metal diphosphides XP<sub>2</sub> (X=Mo, W),” *Phys. Rev. Lett.* **117**, 066402 (2016).
- [42] Arash A. Mostofi, Jonathan R. Yates, Young-Su Lee, Ivo Souza, David Vanderbilt, and Nicola Marzari, “wannier90: A tool for obtaining maximally-localised wannier functions.” *Computer Phys. Comm.* **178**, 685–699 (2008).
- [43] Arash A Mostofi, Jonathan R Yates, Giovanni Pizzi, Young-Su Lee, Ivo Souza, David Vanderbilt, and Nicola Marzari, “An updated version of wannier90: A tool for obtaining maximally-localised wannier functions,” *Computer Phys. Comm.* **185**, 2309–2310 (2014).